Experimental Results on Two-Photon Physics from LEP

Richard Nisius

CERN, CH-1211 Genève 23, Switzerland

Abstract. This review covers selected results from the LEP experiments on the structure of quasi-real and virtual photons. The topics discussed are the total hadronic cross-section for photon-photon scattering, hadron production, jet cross-sections, heavy quark production for photon-photon scattering, photon structure functions, and cross-sections for the exchange of two virtual photons.

1 Introduction

The photon structure has been investigated in detail at LEP based on the scattering of two electrons[1] proceeding via the exchange of two photons, as shown in Figure 1. The reactions are classified depending on the virtualities of the pho-

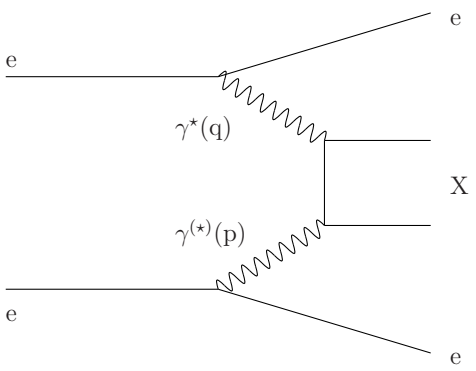

Fig. 1. A diagram of the reaction ee $\rightarrow$ ee$X$, proceeding via the exchange of two photons.

tons, with $-q^2 = Q^2$ and $-p^2 = P^2$, and on the nature of the final state X. If a photon has small virtuality, and the corresponding electron is not observed in the experiment, it is called a quasi-real photon, γ. If the electron is observed,

[1] Fermions and anti-fermions are not distinguished, for example, electrons and positrons are referred to as electrons. The natural system of units, which means, $c = \hbar = 1$ is used.

the photon is far off-shell, and the virtual photon is denoted with $\gamma^\star$. As the two photons can either be quasi-real or virtual the reactions are classified as $\gamma\gamma$ scattering (photon-photon scattering or anti-tagged events), $\gamma\gamma^\star$ scattering (deep inelastic electron-photon scattering or single tag events), and $\gamma^\star\gamma^\star$ scattering (double tag events). In each of the classes, different aspects of the photon structure can be investigated. Due to space limitations not all results can be reviewed here, only a personal selection has been chosen driven by the relevance of the different topics in the context of this workshop on HERA physics. The main results not covered here concern resonance production and glueball searches, which are described in Ref. [1].

2 Results from $\gamma\gamma$ Scattering

The $\gamma\gamma$ scattering reaction has the largest hadronic cross-section at LEP2 energies. The main topics studied are the total hadronic cross-section for photon-photon scattering, $\sigma_{\gamma\gamma}$, and more exclusively, hadron production, jet cross-sections and the production of heavy quarks.

2.1 The Total Photon-Photon Cross-Section

The measurement of $\sigma_{\gamma\gamma}$ is both, interesting and challenging. It is interesting, because in the framework of Regge theory $\sigma_{\gamma\gamma}$ can be related to the total hadronic cross-sections for photon-proton and hadron-hadron scattering, $\sigma_{\gamma\mathrm{p}}$ and σ_{hh}, and a slow rise with the photon-photon center-of-mass energy, $s = W^2$, is predicted. It is challenging, firstly, because experimentally the determination of the hadronic invariant mass, W, is very difficult due to limited acceptance and resolution for the hadrons created in the reaction and secondly, because the composition of different event classes, for example, diffractive and quasi-elastic processes, is rather uncertain, which affects the overall acceptance of the events. The first problem is dealt with by determining W from the visible hadronic invariant mass using unfolding programs. The second uncertainty is taken into account by using two models, namely PHOJET [2] and PYTHIA [3], for the description of the hadronic final state and for the correction from the accepted cross-section to $\sigma_{\gamma\gamma}$, leading to the largest uncertainty of the result.

The published measurements of $\sigma_{\gamma\gamma}$ by L3 [4] and by OPAL [5] are shown in Figure 2(left). Both results show a clear rise as a function of W. The cross-section $\sigma_{\gamma\gamma}$ is interpreted within the framework of Regge theory, motivated by the fact that $\sigma_{\gamma\mathrm{p}}$ and σ_{hh} are well described by Regge parametrisations using terms to account for pomeron and reggeon exchanges. The originally proposed form of the Regge parametrisation for $\sigma_{\gamma\gamma}$ is

$$\sigma_{\gamma\gamma}(s) = X_{1\gamma\gamma} s^{\epsilon_1} + Y_{1\gamma\gamma} s^{-\eta_1} \,, \tag{1}$$

where s is taken in units of GeV^2. The first term in the equation is due to soft pomeron exchange and the second term is due to reggeon exchange. The

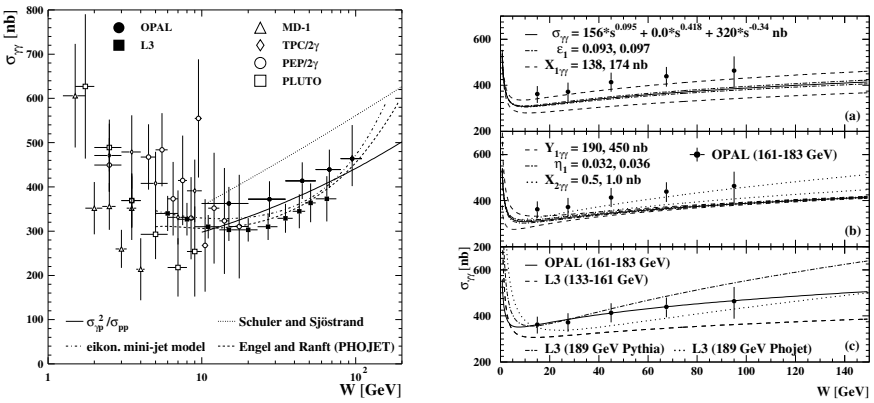

Fig. 2. The published results on $\sigma_{\gamma\gamma}$ as a function of W (right), and an illustration of the spread of the fit results to various data (left).

exponents ϵ_1 and η_1 are assumed to be universal. The presently used values of $\epsilon_1 = 0.095 \pm 0.002$ and $\eta_1 = 0.034 \pm 0.02$ are taken from Ref. [6]. The parameters were obtained by a fit to the total hadronic cross-sections of pp, $p\bar{p}$, $\pi^{\pm}$p, $K^{\pm}$p, γp and $\gamma\gamma$ scattering reactions. The coefficients $X_{1\gamma\gamma}$ and $Y_{1\gamma\gamma}$ have to be extracted from the $\gamma\gamma$ data. The values obtained in Ref. [6] by a fit to older $\gamma\gamma$ data, including those of L3 from Ref. [4], are $X_{1\gamma\gamma} = (156 \pm 18)$ nb and $Y_{1\gamma\gamma} = (320 \pm 130)$ nb. Recently an additional hard pomeron component has been suggested in Ref. [7] leading to

$$\sigma_{\gamma\gamma}(s) = X_{1\gamma\gamma} s^{\epsilon_1} + X_{2\gamma\gamma} s^{\epsilon_2} + Y_{1\gamma\gamma} s^{-\eta_1} \,, \tag{2}$$

with a proposed value of $\epsilon_2 = 0.418$ and an expected uncertainty of ϵ_2 of about ± 0.05. Different fits to the data have been performed by the experiments.

The interpretation of the results is very difficult, because, firstly the parameters are highly correlated, secondly, the main region of sensitivity to the reggeon term is not covered by the OPAL measurement and thirdly, different assumptions have been made when performing the fits. The correlation of the parameters of Eq. (2) can be clearly seen in Figure 2(right a,b), where the theoretical predictions are shown, exploring the uncertainties for the soft pomeron term in (a) and for the reggeon as well as for the hard pomeron term in (b), using the central values and errors quoted in Ref. [6]. It is clear from Figure 2(right a,b) that by changing different parameters in (a) and (b) a very similar effect on the rise of the total-cross section can be achieved. Figure 2(right c) shows the spread of the best fit curves for various data and various fit assumptions explained below. In Figure 2(right a-c) in addition the results from Ref. [5] are shown to illustrate the size of the experimental uncertainties.

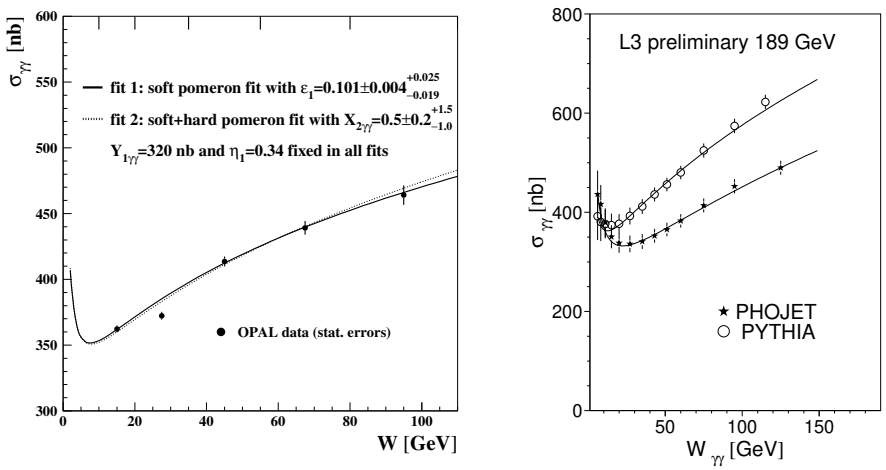

Fig. 3. Fits to the total hadronic cross-section for photon-photon scattering as a function of W for OPAL data at $\sqrt{s}_{\rm ee} = 161 - 189$ GeV (left), and for L3 data at $\sqrt{s}_{\rm ee} = 189$ GeV using two different Monte Carlo models for correcting the data (right).

Examples of different fits are shown in Figure 3 taken from Refs. [5,8]. They yield the following results:

• The OPAL data, within the present range of W, can be accounted for without the presence of the hard pomeron term. When fixing all exponents and $Y_{1\gamma\gamma}$ to the values listed above the fit yields $X_{2\gamma\gamma} = (0.5 \pm 0.2^{+1.5}_{-1.0})$ nb, which is not significantly different from zero, and $X_{1\gamma\gamma} = (182 \pm 3 \pm 22)$ nb, which is consistent with the values from Ref. [6]. Using $X_{2\gamma\gamma} = 0$ and leaving only ϵ_1 and $X_{1\gamma\gamma}$ as free parameters results in $\epsilon_1 = 0.101 \pm 0.004^{+0.025}_{-0.019}$ and $X_{1\gamma\gamma} = (180 \pm 5^{+30}_{-32})$ nb, Figure 2(right, c, full), again consistent with Ref. [6].

• In all fits performed by L3 the hard pomeron term is set to zero. The L3 data from Ref. [4] can be fitted using the old values for the exponents of $\epsilon_1 = 0.0790 \pm 0.0011$ and $\eta_1 = 0.4678 \pm 0.0059$ from Ref. [9] leading to $X_{1\gamma\gamma} = (173 \pm 7)$ nb and $Y_{1\gamma\gamma} = (519 \pm 125)$ nb, Figure 2(right, c, dash). The L3 data at $\sqrt{s}_{\rm ee} = 189$ GeV indicate a faster rise with energy. Using $\epsilon_1 = 0.95$ and $\eta_1 = 0.34$, and the PHOJET Monte Carlo for correcting the data, leads to $X_{1\gamma\gamma} = (172 \pm 3)$ nb and $Y_{1\gamma\gamma} = (325 \pm 65)$ nb, but the confidence level of the fit is only 0.000034 [8]. Fixing only the reggeon exponent to $\eta_1 = 0.34$ leads to $\epsilon_1 = 0.222 \pm 0.019/0.206 \pm 0.013$, $X_{1\gamma\gamma} = (50 \pm 9)\,/\,(78 \pm 10)$ nb and $Y_{1\gamma\gamma} = (1153 \pm 114)\,/\,(753 \pm 116)$ nb, when using PHOJET/PYTHIA, Figure 2(right, c, dot/dot-dash).

In summary, the situation is unclear at the moment with OPAL being consistent with the universal Regge prediction, whereas L3 indicating a faster rise with s for the data at $\sqrt{s}_{\rm ee} = 189$ GeV. In addition, the L3 data taken at different center-of-mass energies show a different behaviour of the measured cross-

section, with the data taken at $\sqrt{s}_{\rm ee} = 133 - 161$ GeV being lower, especially for $W < 30$ GeV.

2.2 The Production of Charged Hadrons

The production of charged hadrons is sensitive to the structure of the photon-photon interactions without theoretical and experimental problems related to the definition and reconstruction of jets. The two main results from the study of hadron production at LEP are shown in Figure 4.

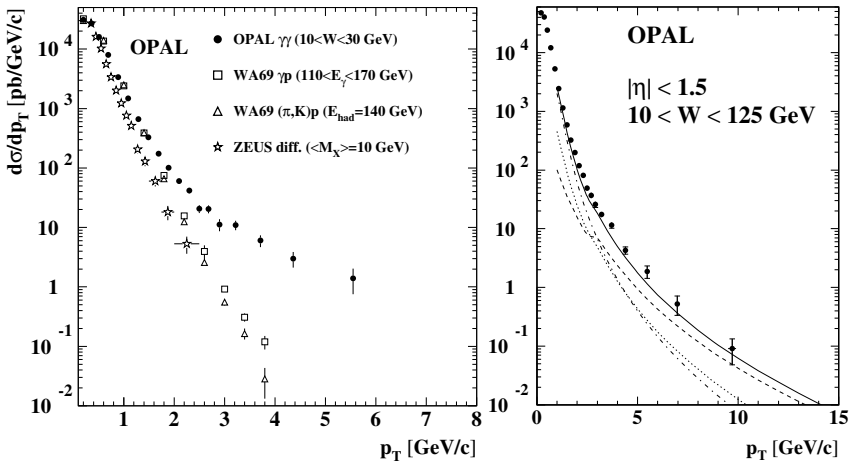

Fig. 4. The differential single particle inclusive cross-section for hadron production in photon-photon scattering at $\sqrt{s}_{\rm ee} = 161 - 172$ GeV compared to other experiments for $10 < W < 30$ GeV (left), and compared to next-to-leading order calculations for $10 < W < 125$ GeV (right).

In Figure 4(left) the differential single particle inclusive cross-section $\mathrm{d}\sigma/\mathrm{d}p_{\rm T}$ for charged hadrons for $\gamma\gamma$ scattering as obtained by OPAL [10], with $10 < W < 30$ GeV, is shown, together with results from γp, πp and Kp scattering from WA69 with a hadronic invariant mass of 16 GeV. The WA69 data are normalised to the $\gamma\gamma$ data at $p_{\rm T} \approx 0.2$ GeV. In addition, ZEUS data from Ref. [11] on charged particle production in γp scattering with a diffractively dissociated photon are shown. These data have an average invariant mass of the diffractive system of 10 GeV, and again they are normalised to the OPAL data. In Figure 4(right) the differential single particle inclusive cross-section for $10 < W < 125$ GeV is compared to next-to-leading order QCD predictions. The main findings are:

- The spectrum of transverse momentum of charged hadrons in photon-photon scattering is much harder than in the case of photon-proton, hadron-proton and 'photon-Pomeron' interactions. This can be attributed to the direct component of the photon-photon interactions.

• The production of charged hadrons is found to be well described by the next-to-leading order QCD predictions from Ref. [12] over a wide range of W. These next-to-leading order calculations are based on the QCD partonic cross-sections, the next-to-leading order GRV parametrisation of the parton distribution functions and on fragmentation functions fitted to e^+e^- data. The renormalisation and factorisation scales are set equal to p_T.

2.3 Jet Production

Jet production is the classical way to study the partonic structure of particle interactions. At LEP the di-jet cross-section in $\gamma\gamma$ scattering was studied in Ref. [13] at $\sqrt{s}_{ee} = 161-172$ GeV using the cone jet finding algorithm with $R = 1$. Three event classes are defined, direct, single-resolved and double-resolved interactions. Here, direct means that the photons as a whole take part in the hard interaction, whereas resolved means that a parton of a hadronic fluctuation of the photon participates in the hard scattering reaction. Experimentally, direct and double-resolved interactions can be clearly separated using the quantity

$$x_\gamma^\pm = \frac{\sum_{\text{jets}=1,2}(E \pm p_z)}{\sum_{\text{hadrons}}(E \pm p_z)}, \tag{3}$$

whereas a selection of single-resolved events cannot be achieved with high purity. Ideally, in leading order direct interactions have $x_\gamma^\pm = 1$, however, due to resolution and higher order corrections the measured values of $x_\gamma^\pm$ are smaller. Experimentally, samples containing large fractions of direct events can be selected by requiring $x_\gamma^\pm > 0.8$, and samples containing large fractions of double-resolved events by using $x_\gamma^\pm < 0.8$.

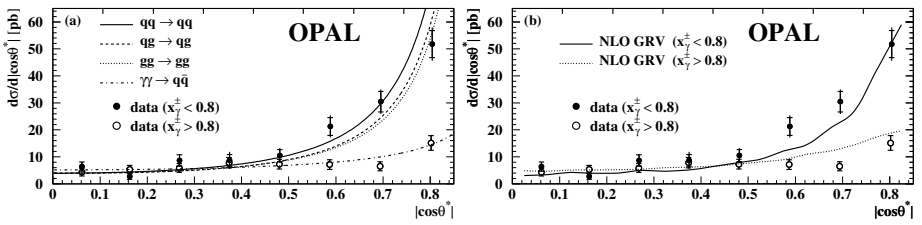

Fig. 5. The angular dependence of di-jet production at $\sqrt{s}_{ee} = 161-172$ GeV compared to leading order matrix elements (left) and to next-to-leading order (NLO) predictions (right).

The measurement of the distribution of $\cos\theta^\star$, the cosine of the scattering angle in the photon-photon centre-of-mass system, allows for a test of the different matrix elements contributing to the reaction. The scattering angle is calculated from the jet rapidities in the laboratory frame using

$$\cos\theta^\star = \tanh\frac{\eta^{\text{jet1}} - \eta^{\text{jet2}}}{2}. \tag{4}$$

In leading order the direct contribution $\gamma\gamma \to q\bar{q}$ leads to an angular dependence of the form $(1 - \cos^2\theta^\star)^{-1}$, whereas double-resolved events, which are dominated by gluon induced reactions, are expected to behave approximately as $(1 - \cos^2\theta^\star)^{-2}$. The steeper angular dependence of the double-resolved interactions can be clearly seen in Figure 5(left), where the shape of the di-jet cross-section, for events with di-jet masses above 12 GeV and average rapidities of $|(\eta_1 + \eta_2)/2| < 1$, is compared to leading order predictions. In addition, the shape of the angular distribution observed in the data is roughly described by the next-to-leading order prediction from Refs. [14], Figure 5(right). In both cases the theoretical predictions are normalised to the data in the first three bins.

These next-to-leading order calculations well account for the observed inclusive differential di-jet cross-section, $\mathrm{d}\sigma/\mathrm{d}E_{\mathrm{T}}^{\mathrm{jet}}$, as a function of jet transverse energy, $E_{\mathrm{T}}^{\mathrm{jet}}$, for di-jet events with pseudorapidities $|\eta^{\mathrm{jet}}| < 2$. As expected the

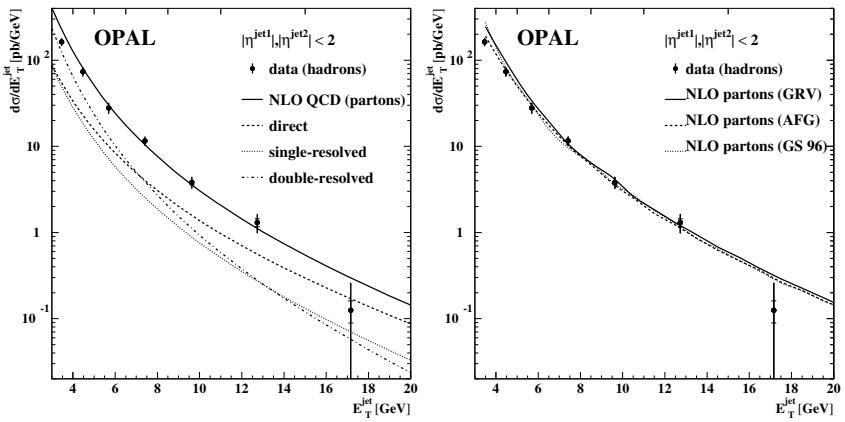

Fig. 6. The $E_{\mathrm{T}}^{\mathrm{jet}}$ dependence of di-jet production at $\sqrt{s}_{\mathrm{ee}} = 161 - 172$ GeV compared to next-to-leading order (NLO) predictions for different event classes (left) and for different parametrisations of the parton distribution functions of the photon (right).

direct component can account for most of the cross-section at large $E_{\mathrm{T}}^{\mathrm{jet}}$, whereas the region of low $E_{\mathrm{T}}^{\mathrm{jet}}$ is dominated by the double-resolved contribution, shown in Figure 6(left). The calculations from Refs. [15] for three different next-to-leading order parametrisations of the parton distribution functions of the photon are in good agreement with the data shown in Figure 6(right), except in the first bin, where theoretical as well as experimental uncertainties are large. Unfortunately, this is the region which shows the largest sensitivity to the differences of the parton distribution functions of the photon.

2.4 Heavy Quark Production

The production of heavy quarks in photon-photon scattering is dominated by charm quark production, as the bottom quarks are much heavier and have a

smaller electric charge. Due to the large scale of the process provided by the charm quark mass, the production of charm quarks can be predicted in next-to-leading order perturbative QCD. In QCD the production of charm quarks at LEP2 energies receives contributions of about equal size from the direct production mechanism and from the single-resolved contribution, shown in Figure 7. In contrast, the double-resolved contribution is expected to be very small, see Ref. [16] for details.

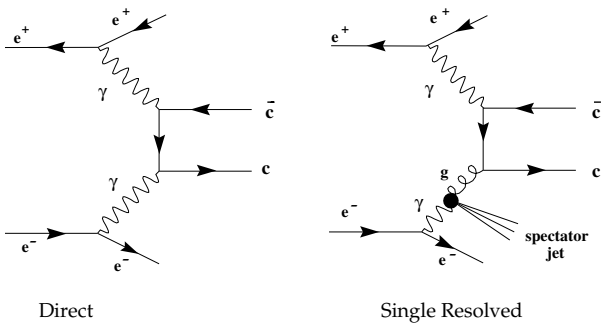

Fig. 7. The direct (left) and single-resolved (right) contributions to charm quark production in photon-photon collisions.

In photon-photon collisions the charm quarks have been tagged using standard techniques, either based on the observation of semileptonic decays of charm quarks using identified electrons and muons in Ref. [17], or by the measurement of $D^\star$ production in Refs. [18–20] using the decay $D^\star \to D^0\pi$, where the pion has very low energy, followed by the D^0 decay observed in one of the decay channels, $D^0 \to K\pi, K\pi\pi^0, K\pi\pi\pi$. The leptons as well as the $D^\star$ can be clearly separated from background processes, as shown in Figure 8. Using the ratio of the transverse energy of the electron measured in the calorimeter and the transverse momentum measured in the tracking chamber the electrons can be well separated from other charged particles, Figure 8(left) from Ref. [17]. Utilising the low energy of the slow pion a clear peak can be observed in the mass difference, ΔM, between the mass of the $D^\star$ and the mass of the D^0 candidate, as shown in Figure 8(right) from Ref. [19]. However, due to the small branching ratios and selection inefficiencies the selected event samples are small and the measurements are limited mainly by the statistical error.

Based on these tagging methods differential cross-sections for charm quark production and $D^\star$ production in restricted kinematical regions have been obtained, examples of which are shown in Figure 9. Figure 9(left) shows the differential cross-section for charm quark production, with semileptonic decays into electrons fulfilling $|\cos\theta_\mathrm{e}| < 0.9$ and $E_\mathrm{e} > 0.6$ GeV and for $W > 3$ GeV. The data are compared to the leading order prediction from PYTHIA, normalised to the number of data events observed. The shape of the distribution is well reproduced by the leading order prediction. Figure 9(right) shows the differential

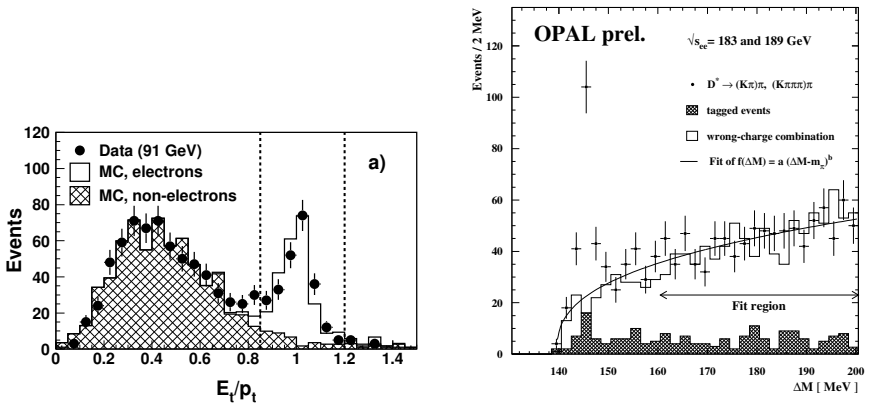

Fig. 8. Charm quark tagging via electrons from semileptonic decays (left), and via the mass difference between the mass of the $D^\star$ and the mass of the D^0 candidate (right).

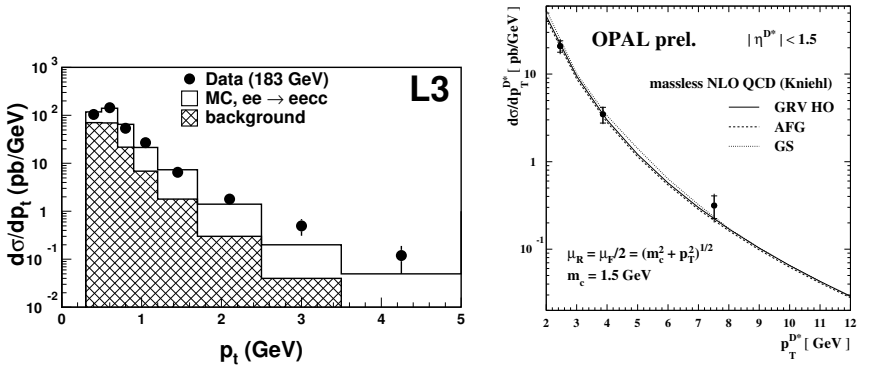

Fig. 9. Differential cross-sections for charm quark production with semileptonic decays into electrons (left), and for $D^\star$ production (right), both determined in restricted kinematical regions.

cross-sections for $D^\star$ production as a function of the transverse momentum of the $D^\star$, for $|\eta^{D^\star}| < 1.5$ compared to the next-to-leading order predictions from Ref. [21] calculated in the massless approach. The differential cross-sections as functions of the transverse momentum and rapidity of the $D^\star$ are well reproduced by the next-to-leading order perturbative QCD predictions, both for the OPAL results [19] and for the L3 results [20]. The shape of the OPAL data can be reproduced by the NLO calculations from Ref. [16], however, the theoretical predictions are somewhat lower than the data, especially at low values of transverse momentum of the $D^\star$.

Based on the observed cross-sections in the restricted ranges in phase space the total charm quark production cross-section is derived, very much relying on

the Monte Carlo predictions for the unseen part of the cross-section. Two issues are addressed, firstly the relative contribution of the direct and single-resolved processes, and secondly the total charm quark production cross-section. The direct and single-resolved events, for example, as predicted by the PYTHIA Monte Carlo, show a different distribution as a function of the transverse momentum of the $D^\star$ meson, $p_T^{D^\star}$, normalised to the visible hadronic invariant mass, $W_{\rm vis}$, as can be seen in Figure 10(left) from Ref. [19]. This feature has been used to experimentally determine the relative contribution of direct and single-resolved events, which were found to contribute about equally to the cross-section.

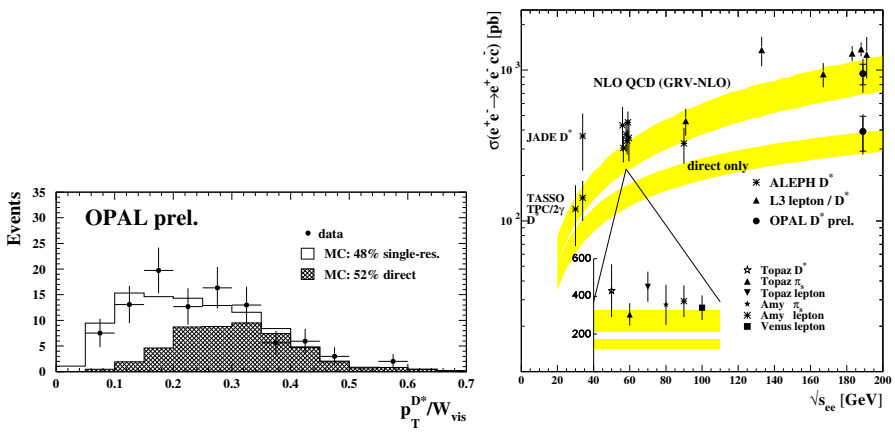

Fig. 10. The separation of the $D^\star$ production into direct and single-resolved contributions (left) and the total cross-section for charm quark production (right).

The total cross-section for the production of charm quarks is shown in Figure 10(right). The LEP results are consistent with each other and the theoretical predictions are in agreement with the data. The measurements suffer from additional errors due to the assumptions made in the extrapolation from the accepted to the total cross-section, which are avoided by only measuring cross-sections in restricted ranges in phase space. It has been shown in Ref. [16] that the NLO calculations are flexible enough to account for the phase space restrictions of an experimental analysis and that the predicted cross-sections in restricted ranges in phase space are less sensitive to variations of the charm mass and to alterations of the renormalisation as well as the factorisation scale. Given this, more insight into several aspects of charm quark production may be gained by comparing experimental results and theoretical predictions for cross-sections in restricted ranges in phase space.

In addition to the measurements of the charm quark production cross-sections, a preliminary measurement of the cross-section for bottom quark production has been reported in Ref. [22].

3 Results from $\gamma\gamma^\star$ Scattering

In this kinematical region the reaction can be described as deep-inelastic electron-photon scattering and allows for measurements of photon structure functions, similarly to measurements of proton structure functions in the case of electron-proton scattering at HERA. The measurements of photon structure functions have been discussed in detail in the literature and the reader is referred to the most recent review, Ref. [23], and to references therein. Only the main results from the LEP experiments are shortly mentioned here.

• The QED structure function $F_{2,\mathrm{QED}}^{\gamma}$ has been precisely measured using data in the approximate range of average virtualities $\langle Q^2 \rangle$ of $1.5 - 130$ GeV^2. The LEP data are so precise that the effect of the small virtuality P^2 of the quasi-real photon can clearly be established.

• The structure functions $F_{\mathrm{A,QED}}^{\gamma}$ and $F_{\mathrm{B,QED}}^{\gamma}$ give more insight into the helicity structure of the $\gamma\gamma^\star$ interaction. They were obtained from the shape of the distribution of the azimuthal angle between the plane defined by the momentum vectors of the muons and the plane defined by the momentum vectors of the incoming and the deeply inelastically scattered electron. Both structure functions were found to be significantly different from zero, and the recent theoretical predictions from Ref. [24], which take into account the important mass corrections up to $\mathcal{O}(m_\mu^2/W^2)$, are consistent with the measurements.

• The hadronic structure function F_2^γ has been measured using data in the approximate range of average virtualities of $\langle Q^2 \rangle$ of $1.9 - 400$ GeV^2. The general features of the measurements can be described by several parametrisations of F_2^γ. However, the data are precise enough to disfavour those parametrisations which predict a fast rise of F_2^γ at low values of x, driven by large gluon distribution functions.

• The evolution of F_2^γ with Q^2 has been studied in bins of x. The measurements are consistent with each other and a clear rise of F_2^γ with Q^2 is observed. The general trend of the data is followed by the predictions of several parametrisations of F_2^γ. It is an interesting fact that at medium values of x this rise can also be described reasonably well ($\mathcal{O}(15\%)$ accuracy) by the leading order augmented asymptotic prediction detailed in Ref. [25], which uses the asymptotic solution from Ref. [26] for F_2^γ for the light flavour contribution as predicted by perturbative QCD for $\alpha_s(M_Z) = 0.128$.

4 Results from $\gamma^\star\gamma^\star$ Scattering

The QED and the hadronic structure of virtual photons have been studied at LEP. The structure functions of virtual photons can be determined for the situation where one photon has a much larger virtuality than the other, $Q^2 \gg P^2$, by measuring the cross-section for events where both electrons are observed. For the situation where both photons have similar virtualities, $Q^2 \approx P^2$, the structure function picture is no longer applicable and differential cross-sections for the exchange of two highly-virtual photons have been measured instead. The

main results from the LEP experiments are shortly mentioned here, for a more detailed discussion the reader is referred to Ref. [23].

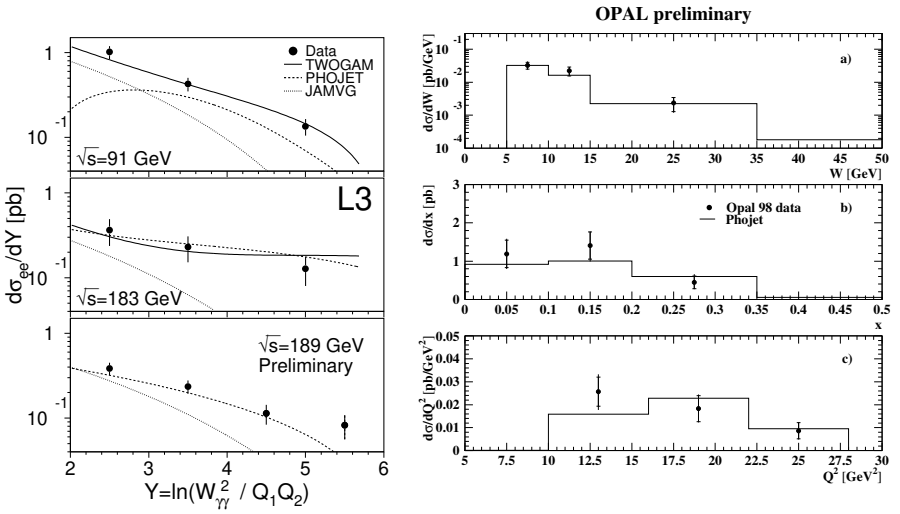

Fig. 11. The differential cross-sections for the exchange of two highly virtual photons as functions of various variables from L3 (left) and OPAL (right).

• The effective hadronic structure function [27] has been measured by L3 [28] for average virtualities of $\langle Q^2 \rangle = 120$ GeV^2 and $\langle P^2 \rangle = 3.7$ GeV^2. A consistent picture is found for the effective structure function between the older PLUTO result from Ref. [27] and the L3 data, and the general features of both measurements are described by the next-to-leading order predictions from Ref. [29].

• The cross-section for the exchange of two highly virtual photons with muon final states has been measured in Ref. [30]. There is good agreement between the measured cross-section and the QED prediction. The measurement shows that the interference terms, which are usually neglected in investigations of the hadronic structure of the photon, are present in the data in the kinematical region of the analysis, mainly at $x > 0.1$, and that the corresponding contributions to the cross-section are negative.

• The cross-section for the exchange of two highly virtual photons with hadronic final states has been measured in Refs. [31–33], and the main results are shown in Figure 11. The differential cross-sections as functions of various variables are well described by leading order Monte Carlo models. Much larger cross-sections are predicted in the framework of BFKL calculations. These predictions are strongly disfavoured by the data.

Acknowledgement

I am grateful to the organisers for inviting me to this inspiring location and for the fruitful atmosphere they created throughout the meeting. I wish to thank Stefan Söldner-Rembold and Bernd Surrow for carefully reading the manuscript and Jochen Patt for providing me with the figure of combined results for the charm quark production cross-section.

References

1. L3 Collaboration, M. Acciarri et al., Phys. Lett. **B363**, 118–126 (1995);
   L3 Collaboration, M. Acciarri et al., Phys. Lett. **B413**, 147–158 (1997);
   L3 Collaboration, M. Acciarri et al., Phys. Lett. **B418**, 399–410 (1998);
   L3 Collaboration, M. Acciarri et al., Phys. Lett. **B453**, 73–82 (1999);
   L3 Collaboration, M. Acciarri et al., CERN-EP/99-072;
   OPAL Collaboration, K. Ackerstaff et al., Phys. Lett. **B439**, 197–208 (1998);
   ALEPH Collaboration, contributed paper to HEP99 Tampere.
2. R. Engel, Z. Phys. **C66**, 203–214 (1995);
   R. Engel and J. Ranft, Phys. Rev. **D54**, 4244–4262 (1996).
3. T. Sjöstrand, Comp. Phys. Comm. **82**, 74–89 (1994).
4. L3 Collaboration, M. Acciarri et al., Phys. Lett. **B408**, 450–464 (1997).
5. OPAL Collaboration, G. Abbiendi et al., CERN-EP/99-076.
6. Particle Data Group, Eur. Phys. J. **C3**, 1–794 (1998).
7. A. Donnachie and P.V. Landshoff, Phys. Lett. **B437**, 408–416 (1998).
8. L3 Collaboration, A. Csilling, in *Proceedings of Photon '99.*
9. Particle Data Group, Phys. Rev. **D54**, 1– (1996).
10. OPAL Collaboration, K. Ackerstaff et al., Eur. Phys. J. **C6**, 253–264 (1999).
11. ZEUS Collaboration, M. Derrick et al., Z. Phys. **C67**, 227–238 (1995).
12. J. Binnewies, B.A. Kniehl, and G. Kramer, Phys. Rev. **D53**, 6110–6119 (1996).
13. OPAL Collaboration, G. Abbiendi et al., CERN-EP/98-113.
14. M. Klasen, T. Kleinwort, and G. Kramer, Eur. Phys. J. **C1**, 1–105 (1998).
15. M. Klasen, private communication.
16. S. Frixione, M. Krämer, and E. Laenen, hep-ph/9908483.
17. L3 Collaboration, M. Acciarri et al., Phys. Lett. **B453**, 83–93 (1999).
18. ALEPH Collaboration, D. Buskulic et al., Phys. Lett. **B355**, 595–605 (1995).
19. OPAL Collaboration, J. Patt, in *Proceedings of Photon '99.*
20. L3 Collaboration, M. Acciarri et al., CERN-EP/99-106.
21. J. Binnewies, B.A. Kniehl, and G. Kramer, Phys. Rev. **D58**, 014014 (1998).
22. L3 Collaboration, R.R. McNeil, in *Proceedings of Photon '99.*
23. R. Nisius, in *Proceedings of Photon '99*, hep-ex/9907012.
24. R. Nisius and M.H. Seymour, Phys. Lett. **B452**, 409–413 (1999).
25. OPAL Collaboration, K. Ackerstaff et al., Phys. Lett. **B411**, 387–401 (1997).
26. E. Witten, Nucl. Phys. **B120**, 189–202 (1977).
27. PLUTO Collaboration, C. Berger et al., Phys. Lett. **142B**, 119–124 (1984).
28. L3 Collaboration, F.C. Erné, in *Proceedings of Photon '99.*
29. M. Glück, E. Reya, and M. Stratmann, Phys. Rev. **D54**, 5515–5522 (1996).
30. OPAL Collaboration, G. Abbiendi et al., CERN-EP/99-010.
31. L3 Collaboration, M. Acciarri et al., Phys. Lett. **B453**, 333–342 (1999).
32. L3 Collaboration, P. Achard, in *Proceedings of Photon '99.*
33. OPAL Collaboration, M. Przybycień, in *Proceedings of Photon '99.*